

Uncertainty Quantification and Risk Control for Multi-Speaker Sound Source Localization

Vadim Rozenfeld , Bracha Laufer Goldshtein 

Abstract—Reliable Sound Source Localization (SSL) plays an essential role in many downstream tasks, where informed decision making depends not only on accurate localization but also on the confidence in each estimate. This need for reliability becomes even more pronounced in challenging conditions, such as reverberant environments and multi-source scenarios. However, existing SSL methods typically provide only point estimates, offering limited or no Uncertainty Quantification (UQ). We leverage the Conformal Prediction (CP) framework and its extensions for controlling general risk functions to develop two complementary UQ approaches for SSL. The first assumes that the number of active sources is known and constructs prediction regions that cover the true source locations. The second addresses the more challenging setting where the source count is unknown, first reliably estimating the number of active sources and then forming corresponding prediction regions. We evaluate the proposed methods on extensive simulations and real-world recordings across varying reverberation levels and source configurations. Results demonstrate reliable finite-sample guarantees and consistent performance for both known and unknown source-count scenarios, highlighting the practical utility of the proposed frameworks for uncertainty-aware SSL.

Index Terms—Sound Source Localization, Conformal Prediction, Uncertainty Quantification, Risk-Control.

I. INTRODUCTION

ACCURATE Sound Source Localization (SSL) is a fundamental component in a wide range of acoustic and audio signal processing systems, including robot audition [1], camera steering [2], and speech enhancement and separation [3]. In these applications, determining the Direction of Arrival (DOA) or positions of one or more active sources enables downstream modules such as beamforming, source separation, diarization, or navigation, to operate reliably. The demand for robust SSL has only intensified as systems encounter increasingly complex acoustic environments with reverberation, noise, and multiple sources.

A large body of work has focused on developing algorithms capable of estimating SSL under challenging acoustic conditions. Several classical approaches generate likelihood maps over a predefined spatial grid. These include Steered-Response Power with Phase Transform (SRP-PHAT) [4] and Expectation Maximization (EM)-based methods [5], which exploit Time-Difference of Arrivals (TDOAs) between microphone pairs, as well as subspace-based techniques such as Multiple Signal Classification (MUSIC) [6] and Estimation of Signal Parameters via Rotational Invariance Techniques (ESPRIT) [7]. More recently, Deep Neural Network (DNN)-based models have

been proposed and often demonstrate improved performance by learning complex patterns that are difficult to capture with traditional signal processing techniques [8]. Many of these approaches produce spatial likelihood maps by imitating classical localization methods [9], [10], [11], or by formulating the SSL problem as a classification task over a set of classes obtained by discretizing the region of interest [12], [13], [14].

Despite notable progress, most SSL systems operate in a strictly point estimation manner, meaning they output a single estimated location for each detected source, without quantifying the reliability of these estimates. However, errors are unavoidable since noise, reverberation, and interfering signals fundamentally distort the spatial cues on which SSL methods rely. Without a principled measure of UQ, downstream components must either trust the SSL output blindly or rely on heuristic thresholds that provide no statistical guarantees.

Few recent approaches have proposed extracting reliability measures for SSL estimates to detect low-confidence estimates and out-of-distribution samples [12], [14]. In [12], Gaussian label smoothing is used during training, and the predicted peak value is treated as a proxy for reliability, while [14] models output uncertainty via a Dirichlet distribution. Both approaches provide useful reliability indicators, albeit without formal statistical guarantees.

A widely used UQ approach that provides distribution-free finite-sample guarantees is CP [15], [16], [17], which constructs Prediction Intervals (PIs) that contain the true value with a user-specified probability. Few recent attempts were made to apply CP for SSL. For the single-source case, [18] applied CP using several uncertainty surrogates, including Monte-Carlo dropout, model ensembles, and quantile regression. Our prior work combined manifold-based SSL based on Gaussian process regression [19] with CP to efficiently obtain statistically valid PIs [20]. This kernel-based localization approach was replaced by a graph neural network in [21], while constructing valid PIs using an alternative Jackknife+ formulation [22]. In the multi-source setting, [23] assumes a known number of sources and models the conditional multi-source DOA distribution using a Gaussian mixture model parameterized by a neural network (NN), and CP is then applied to obtain PIs from its outputs.

These previous works [18], [20], [21], [23] heavily rely on classical CP, which is tailored exclusively to the binarized Mis-Coverage (MC) loss, namely, the probability that the true value lies outside the PI. Yet, multi-source setups introduce additional and potentially competing losses beyond MC. For instance, errors may arise from failing to detect an existing speaker at all, or from declaring a speaker that does not exist. Moreover, classical CP is suited to calibrating

The authors are with The School of Electrical & Computer Engineering, Tel-Aviv University, Tel-Aviv 6139001, Israel (e-mail: vadim-roz@mail.tau.ac.il; blauffer@tauex.tau.ac.il)

only a single hyperparameter, such as a detection threshold, whereas practical systems involve multiple hyperparameters that must be tuned jointly. In addition, prior UQ frameworks are typically optimized for specific localization methods and do not generalize readily to alternative approaches.

This work addresses these gaps by leveraging recent advances in the CP literature, enabling principled UQ for complex, multi-objective settings that classical CP cannot accommodate. We propose a general UQ framework applicable to any multi-source localization method that produces a likelihood map over a grid of candidate positions. We consider both scenarios in which the number of sources is known or unknown. The key idea is to associate each position estimate with an interpretable confidence information, expressed as prediction region, on a 2D spatial likelihood map that contains the true source location with high probability. When the number of sources is unknown, the framework further enables controlled detection of the correct number of sources. Extensive experimental studies demonstrate the effectiveness of the proposed framework across a wide range of conditions.

Our main contributions are summarized as follows:

- Our proposed frameworks operate on spatial likelihood maps from *any* classical or DNN-based localization method, yielding finite-sample, statistically valid prediction regions containing the true source location with high probability.
- We introduce a method for constructing contiguous prediction regions around each SSL estimate that adapt to the local likelihood landscape, without imposing any geometric or distributional assumptions on the region shape. The size of this region directly quantifies uncertainty, with larger regions indicating lower confidence and vice versa. Such information can naturally inform downstream decision-making.
- For the unknown-source case, beyond classical MC risk control, we additionally provide principled simultaneous control over the risk of failing to detect an existing speaker, while discouraging spurious detections and minimizing the size of the prediction region.
- We evaluate the proposed frameworks on single- and multi-source tasks with both known and unknown number of sources. We consider both classical and DNN-based likelihood maps obtained for simulated environments, and real-world recordings. Our code is publicly available on GitHub.¹

The remainder of the paper is organized as follows. Section II formulates the multi-source localization problem. Section III reviews SSL methods based on constructing spatial likelihood maps. Section IV provides background on CP and risk control extensions. Section V presents the proposed approaches for risk control in settings with known and unknown numbers of sources. Section VI describes experimental setup and results, and Section VII concludes the paper.

II. PROBLEM FORMULATION

We consider a reverberant acoustic enclosure with K static sources, $1 \leq K \leq K_{\max}$, where K is unknown but K_{\max} is known. Let $\{\mathbf{p}_k^*\}_{k=1}^K$ denote the 2D DOAs of the sources,

where $\mathbf{p}_k^* = [\phi_k, \theta_k]^T$, with $\phi_i \in [0, \pi]$ and $\theta_k \in [-\pi, \pi]$ denoting the elevation and azimuth angles, respectively. The signal received at the m -th microphone in the Short-Time Fourier Transform (STFT) domain is expressed as

$$X_m(t, f) = \sum_{k=1}^K A_m(f, \mathbf{p}_k^*) S_k(t, f) + U_m(t, f), \quad (1)$$

where $t \in \{1, \dots, T\}$ and $f \in \{1, \dots, F\}$ denote the frame and frequency indices, respectively. Here, $S_k(t, f)$ is the k -th source signal, $A_m(f, \mathbf{p}_k^*)$ is the Room Impulse Response (RIR) relating the k -th source at \mathbf{p}_k and the m -th microphone, and $U_m(t, f)$ is an additive noise.

Our framework builds on existing SSL methods that produce 2D spatial likelihood maps, from which the DOAs are estimated. We consider both classical approaches, such as SRP-PHAT [4], and neural network-based models [9], [10], [11], [12], [13]. Given a generic spatial likelihood map, our goal is to enable principled UQ and risk control by constructing prediction regions that cover the true source locations with high probability. When the number of sources is unknown, we additionally wish to control the error of incorrectly estimating the source count.

III. BACKGROUND ON SOUND SOURCE LOCALIZATION

This section reviews two representative localization methods that produce 2D spatial likelihood maps: the classical SRP-PHAT method [4] and the learning-based SRP-DNN [10]. Importantly, our frameworks seamlessly generalize to any method capable of producing analogous maps, e.g., [6], [7], [9], [11].

A. SRP-PHAT

Various SSL methods rely on TDOA estimation between pairs of microphones. A prominent example is SRP-PHAT [4], which steers the microphone array over a set of hypothesized phases defined on a spatial grid. This process yields a spatial likelihood map, whose peaks correspond to potential source directions. To construct this map, the phase-normalized cross-correlation is evaluated for each microphone pair (m, m') at every time-frequency (T-F) bin.

$$\Psi_{mm'}(t, f) = \frac{|X_m(t, f)X_{m'}^*(t, f)|}{|X_m(t, f)X_{m'}^*(t, f)|}, \quad (2)$$

where $|\cdot|$ denotes the magnitude of a complex-number. The normalization enforces unit magnitude across frequencies, leaving only phase differences. Then, given a hypothesized direction $\mathbf{p} = [\phi, \theta]^T$, the expected TDOA between a pair of microphones m and m' is

$$\tau_{mm'}(\mathbf{p}) = \frac{(\mathbf{m}_m - \mathbf{m}_{m'})^T \mathbf{u}(\mathbf{p})}{c}, \quad (3)$$

where \mathbf{m}_m and $\mathbf{m}_{m'}$ are the microphone positions, $\mathbf{u}(\mathbf{p}) = [\sin(\phi) \cos(\theta), \sin(\phi) \sin(\theta), \cos(\phi)]^T$ is the unit vector pointing toward the source and c is the speed of sound.

¹https://github.com/vadimroz/UQ_in_multi_SSL

The SRP likelihood map at direction \mathbf{p} is computed using $M(M-1)/2$ non-redundant microphone pairs with $m' > m$ as

$$\Phi_{\text{SRP-PHAT}}(\mathbf{p}) = \frac{2}{M(M-1)} \frac{1}{TF} \sum_{m', m} \sum_{f=1}^F \sum_{t=1}^T \Re \left\{ \Psi_{mm'}(t, f) e^{-j\omega_f \tau_{mm'}(\mathbf{p})} \right\}. \quad (4)$$

where $\Re\{\cdot\}$ denotes the real part, and $\omega_f = 2\pi f$. Multiplying by $e^{-j\omega_f \tau_{mm'}(\mathbf{p})}$ virtually steers the microphone pair (m, m') towards candidate direction. Averaging across T-F bins and microphone pairs produces a spatial likelihood map $\Phi_{\text{SRP-PHAT}}$ whose peaks indicate the most probable source directions.

B. SRP-DNN

Classic SSL algorithms often struggle when multiple sources are simultaneously active, as interference can lead to less pronounced spatial peaks, peak merging, or even spurious responses. Reverberation and ambient noise further exacerbate these issues, making accurate source detection and localization increasingly difficult. To this end, the SRP-DNN [10] uses a deep learning model designed to suppress acoustic interference and estimate the direct-path Inter-Channel Phase Differences (IPDs) for each microphone pair (m, m') , given by:

$$\text{IPD}_{mm'}(f; \mathbf{p}^*) = e^{j\omega_f \tau_{mm'}(\mathbf{p}^*)}. \quad (5)$$

Note that in anechoic, noise-free rooms, the phase-normalized cross-correlation defined in (2) satisfies $\Psi_{mm'}(t, f) = \text{IPD}_{mm'}(f; \mathbf{p}^*)$ for a true source located at \mathbf{p}^* . Consequently, the likelihood in (4) is maximized whenever $\mathbf{p} = \mathbf{p}^*$.

At its core, SRP-DNN adopts a Convolutional Recurrent Neural Network (CRNN) to extract IPDs from noisy and reverberant microphone signals. Let $\mathbf{r}_{mm'}(\mathbf{p}^*) \in \mathbb{R}^{2F \times 1}$ denote the real-valued vector form of the direct-path IPD

$$\mathbf{r}_{mm'}(\mathbf{p}^*) = [\cos(\omega_1 \tau_{mm'}(\mathbf{p}^*)), \sin(\omega_1 \tau_{mm'}(\mathbf{p}^*)), \dots, \cos(\omega_F \tau_{mm'}(\mathbf{p}^*)), \sin(\omega_F \tau_{mm'}(\mathbf{p}^*))]^T. \quad (6)$$

The model is trained to estimate a summed direct-path IPD representation encoding the contributions of all K sources

$$\mathbf{R}_{mm'}(t) = \sum_{k=1}^K \pi_k(t) \mathbf{r}_{mm'}(\mathbf{p}_k^*), \quad (7)$$

where $\pi_k(t) \in [0, 1]$ denotes the activity probability of the k -th source at the t -th frame. The SRP-DNN model is optimized by minimizing the mean squared error (MSE) between the prediction $\hat{\mathbf{R}}_{mm'}(t)$ and the training target at (7). Analogously to (4), the spatial likelihood map is given by

$$\Phi_{\text{SRP-DNN}}(\mathbf{p}) = \frac{2}{M(M-1)} \frac{1}{TF} \sum_{t=1}^T \sum_{m', m} \hat{\mathbf{R}}_{mm'}(t)^T \mathbf{r}_{mm'}(\mathbf{p}). \quad (8)$$

C. Source Localization from the Likelihood Map

We now describe how to extract source position estimates from a given spatial likelihood map (e.g., as defined in (4)

Algorithm 1 Iterative Source Detection and Localization

Input: Spatial grid \mathcal{G} , likelihood maps $\Phi(\mathbf{p})$ for $\mathbf{p} \in \mathcal{G}$; Stopping threshold β_{TH} and maximum count K_{max} or known count K ; Minimum separation d , and method $\in \{\text{SRP-PHAT}, \text{SRP-DNN}\}$.

Output: Detected DOAs $\{\hat{\mathbf{p}}_1, \dots, \hat{\mathbf{p}}_k\}$ and the corresponding likelihood maps $\{\Phi^{(1)}, \dots, \Phi^{(k)}\}$

```

1: Initialize  $\Phi^{(1)}(\mathbf{p}) \leftarrow \Phi(\mathbf{p})$ 
2: Initialize  $\mathcal{F}_1 \leftarrow \mathcal{G}$ 
3: for  $k \leftarrow 1$  to  $K_{\text{max}}$  do  $\triangleright$  or  $K$  loops at known count
4:    $\hat{\mathbf{p}}_k \leftarrow \arg \max_{\mathbf{p} \in \mathcal{F}_k} \Phi^{(k)}(\mathbf{p})$ 
5:   if  $\Phi^{(k)}(\hat{\mathbf{p}}_k) < \beta_{\text{TH}}$  then  $\triangleright$  only for unknown count
6:     break
7:   end if
8:    $\hat{\beta}_k \leftarrow \Phi^{(k)}(\hat{\mathbf{p}}_k)$ 
9:   if method = SRP-PHAT then
10:      $\Psi_{mm'}^{(k+1)}(t, f) \leftarrow \Psi_{mm'}^{(k)}(t, f) - \hat{\beta}_k \cdot e^{j\omega_f \tau_{mm'}(\hat{\mathbf{p}}_k)}$ 
11:   else if method = SRP-DNN then
12:      $\hat{\mathbf{R}}_{mm'} \leftarrow \hat{\mathbf{R}}_{mm'} - \hat{\beta}_k \cdot \mathbf{r}_{mm'}(\hat{\mathbf{p}}_k)$ 
13:   end if
14:   UPDATE  $\Phi^{(k+1)}$   $\triangleright$  Eq. (4) or (8)
15:    $\mathcal{F}_{k+1} \leftarrow \{\mathbf{p} \in \mathcal{G} : |\phi - \hat{\phi}_i| \geq d \wedge |\theta - \hat{\theta}_i| \geq d, \forall i < k\}$ 
16: end for
17: return  $\{\hat{\mathbf{p}}_1, \dots, \hat{\mathbf{p}}_k\}, \{\Phi^{(1)}, \dots, \Phi^{(k)}\}$ 

```

and (8)). In the single-source case, the estimated position can be simply determined by the peak of the likelihood map

$$\hat{\mathbf{p}} = \arg \max_{\mathbf{p} \in \mathcal{G}} \Phi(\mathbf{p}), \quad (9)$$

where \mathcal{G} denotes a grid of candidate directions. In practice, overlapping sources and adverse acoustic conditions make the estimator in (9) unsuitable for directly recovering multiple active sources. An alternative approach, as explored in [10], [24], [25], [26], is to iteratively detect the dominant source from the likelihood map Φ using (9), suppress its spatial contribution, and then re-estimate the map to uncover new sources. Since the true number of sources is often unknown, stopping criterion becomes an essential design component. For example, in [10], the process halts when the global maximum of the likelihood map falls below a predefined threshold, whereas [24] uses a sparsity-based criterion derived from the GCC function, terminating the procedure when the kurtosis value becomes sufficiently small. However, the exact stopping threshold is often determined heuristically without any performance guarantees.

We adopt a standard iterative detection-localization procedure [10], as summarized in Algorithm 1. When the source count is known the algorithm stops exactly after K iterations, while in the unknown case, the termination is based on thresholding. In Section V, we show that this threshold can be selected through a principled risk controlling framework.

We note that although Algorithm 1 is presented in the context of SRP-type methods, the UQ frameworks developed in this paper are general. They can be readily adapted, with only minor modifications, to any SSL approach yielding a sequence of detected DOAs and their corresponding likelihood maps.

D. Uncertainty Quantification

A key limitation of many SSL methods is that they yield only point estimates, offering no indication of confidence. Incorporating UQ is therefore highly beneficial, as it enables more informed downstream decisions by quantifying the confidence in each localization result. In the context of SSL, uncertainty can be naturally expressed using prediction regions constructed directly on top of the spatial likelihood map. In particular, a more compact region indicates higher confidence in the corresponding localization estimate. When the number of sources is unknown, we would like to account also for the uncertainty in detecting the correct number of sources. To enable statistical guarantees for prediction coverage and reliable control over missed detections, our framework relies on CP and its extensions. The following section provides a detailed background on these methods.

IV. BACKGROUND ON CONFORMAL PREDICTION

A. Overview

In recent years, CP [15], [16], [17] has gained popularity as it provides a distribution-free framework for constructing predictive intervals with finite-sample guarantees, independent of the underlying model or data distribution. Its appeal stems from being a generic post-hoc approach that requires only data exchangeability, i.e., the joint distribution of data samples is invariant under any permutation. This generality has enabled successful applications primarily in computer vision [27], [28] and natural language processing [29], [30], and more recently in speech processing [18], [20], [21], [23].

Split CP [16], [31] is a practical variant of CP that employs a simple data-splitting scheme. The available samples are divided into a training set, used to fit a predictive model \hat{f} , and a separate calibration set $\mathcal{D}_{\text{cal}} = \{(X_i, Y_i)\}_{i=1}^n, (X_i, Y_i) \sim \mathcal{P}$, where \mathcal{P} is an arbitrary distribution on $\mathcal{X} \times \mathcal{Y}$. In this context, $X_i \in \mathcal{X}$ denotes a feature vector and $Y_i \in \mathcal{Y}$ the corresponding response. Given a fresh test pair $(X_{n+1}, Y_{n+1}) \sim \mathcal{P}$, the goal is to construct a statistically valid PI, i.e., $\mathcal{C}(X_{n+1})$, that contains the unobserved response Y_{n+1} with high probability. To this end, a nonconformity score function $s(x, y) \in \mathbb{R}$ is used to measure the agreement between y and x based on a trained model \hat{f} . Better consistency leads to a smaller score. The choice of the nonconformity score is task-dependent, but a common choice for regression problems is the residual error function $s(x, y) = |y - \hat{f}(x)|$. Let $s_i = s(X_i, Y_i)$ denote the score associated with the i -th calibration sample, the prediction interval for an unseen feature vector X_{n+1} is

$$\mathcal{C}(X_{n+1}) = [\hat{f}(X_{n+1}) - \hat{q}_{1-\alpha}, \hat{f}(X_{n+1}) + \hat{q}_{1-\alpha}], \quad (10)$$

where $\hat{q}_{1-\alpha}$ is the $(1-\alpha)(1+1/n)$ -quantile of the calibration scores $\{s_1, \dots, s_n\}$. Under the sole assumption that the calibration and test samples $\{(X_i, Y_i)\}_{i=1}^{n+1}$ are exchangeable, split CP [16] provides a finite-sample coverage guarantee:

$$\mathbb{P}(Y_{n+1} \in \mathcal{C}(X_{n+1})) \geq 1 - \alpha. \quad (11)$$

By the law of total expectation, this is equivalent to $\mathbb{E}[\mathbb{1}\{Y_{n+1} \notin \mathcal{C}(X_{n+1})\}] \leq \alpha$ with an expectation over the MC loss $\mathbb{1}\{Y_{n+1} \notin \mathcal{C}(X_{n+1})\}$.

B. Conformal Risk Control

While CP controls the MC loss, it may not be the most natural choice for many tasks. Conformal Risk Control (CRC) [32] extends CP to arbitrary bounded loss functions $L(\lambda)$ that are non-increasing in a tuning parameter $\lambda \in \Lambda \subset \mathbb{R} \cup \{\pm\infty\}$, meaning $L(\lambda_2) \leq L(\lambda_1)$ for $\lambda_1 < \lambda_2$. Subsequently, the associated risk function is defined as

$$\mathcal{R}(\lambda) = \mathbb{E}[L(\lambda)], \quad \lambda \in \Lambda, \quad (12)$$

assuming the existence of $\lambda_{\min} \in \Lambda$ such that $\mathcal{R}(\lambda_{\min}) = 0$.

Let the random variables $L_i : \Lambda \rightarrow (-\infty, B]$ for $i = 1, \dots, n+1$ be defined by $L_i(\lambda) = L(X_i, Y_i; \lambda)$ and define the corresponding empirical risk over the calibration data as

$$\hat{\mathcal{R}}_n(\lambda) = \frac{1}{n} \sum_{i=1}^n L_i(\lambda). \quad (13)$$

Given a target risk tolerance $\alpha \in (-\infty, B)$, the CRC procedure selects the threshold

$$\hat{\lambda} = \inf \left\{ \lambda : \hat{\mathcal{R}}_n(\lambda) \leq \alpha - \frac{B-\alpha}{n} \right\}, \quad (14)$$

which controls the risk on unseen data as stated in the following Theorem.

Theorem 1 (Conformal Risk Control [32]). *Suppose $L_i(\lambda)$ is non-increasing in λ , right-continuous, satisfying $L_i(\mathcal{C}_{\lambda_{\max}}) \leq \alpha$ for $\lambda_{\max} = \sup \Lambda \in \Lambda$ and $\sup_{\lambda} L_i(\lambda) \leq B < \infty$ almost surely. Then $\mathbb{E}[L_{n+1}(\hat{\lambda})] \leq \alpha$.*

C. Advanced Risk-Control Methods

CRC controls monotonic risks at level α , but a stronger version would provide high-probability risk control

$$\mathbb{P}(\mathcal{R}(\lambda) \leq \alpha) \geq 1 - \delta. \quad (15)$$

meaning that with at least $1 - \delta$ probability, any drawn calibration set \mathcal{D}_{cal} yields an expected loss that does not exceed the risk limit α . Indeed, Risk-Controlling Prediction Set (RCPS) [33], [34] offers a rigorous method for constructing prediction functions that achieves the property at (15). Learn Then Test (LTT) [35] extends RCPS by removing the monotonicity requirement on the risk and enabling the calibration of multi-dimensional threshold configurations, $\boldsymbol{\lambda} = (\lambda_1, \dots, \lambda_D)$ defined over a continuous space $\Lambda = \Lambda_1 \times \dots \times \Lambda_D$. This allows simultaneous control of multiple risks, $\mathcal{R}_\ell \leq \alpha_\ell$ for $\ell = 1, \dots, N_c$. The key idea is to cast the configuration selection as a Multiple Hypothesis Testing (MHT) procedure, testing a finite set of configurations $\Lambda_g \subseteq \Lambda$. For each configuration $\boldsymbol{\lambda}_j \in \Lambda_g$ consider the null hypothesis

$$\mathcal{H}_j : \exists \ell \in \{1, \dots, N_c\} \text{ such that } \mathcal{R}_\ell(\boldsymbol{\lambda}_j) > \alpha_\ell. \quad (16)$$

By construction, *rejecting* \mathcal{H}_j certifies that, for configuration $\boldsymbol{\lambda}_j$, all risks are controlled, i.e., $\mathcal{R}_\ell(\boldsymbol{\lambda}_j) \leq \alpha_\ell$ for every ℓ . Let $\Lambda_{\text{rej}} \subseteq \Lambda_g$ denote the true rejection set. The LTT framework provides a principled method for determining an estimated rejection set $\hat{\Lambda}_{\text{rej}} \subseteq \Lambda_g$ based on calibration data. Importantly, it controls the Family-Wise Error Rate (FWER) at level δ , meaning that the probability of making at least one false rejection among all tested hypotheses is bounded by δ .

For constructing the rejection set, we first need to derive a finite-sample valid p -value p , i.e., $\mathbb{P}(p \leq u) \leq u$ for $u \in [0, 1]$ under \mathcal{H}_j (see Appendix A-A for further details). For a given configuration λ_j and risk tolerance α_ℓ , let $p(\{L_i^\ell(\lambda_j)\}_{i \in \mathcal{D}_{\text{cal}}}; \alpha_\ell)$ denote the p -value of the j -th null hypothesis $\mathcal{H}_{j,\ell} : \mathcal{R}_\ell(\lambda_j) > \alpha_\ell$ associated with the ℓ -th loss. The p -value of the aggregated null hypothesis in (16) can be computed as [35]

$$p_j^{\text{cal}} = \max_{\ell=1, \dots, N_c} p(\{L_i^\ell(\lambda_j)\}_{i \in \mathcal{D}_{\text{cal}}}; \alpha_\ell), \quad \lambda_j \in \Lambda_g. \quad (17)$$

Then, whenever $p_j^{\text{cal}} < \delta$, we declare that all risks $\mathcal{R}_\ell(\lambda_j)$, $\ell = 1, \dots, N_c$, are simultaneously controlled.

Given valid p -values, a rejection set $\hat{\Lambda}_{\text{rej}}$ is constructed by applying an FWER-controlling algorithm $\mathcal{A}: [0, 1]^{|\Lambda_g|} \rightarrow 2^{\Lambda_g}$. In essence, the algorithm \mathcal{A} takes as input the collection of p -values and returns a set of rejected configurations $\hat{\Lambda}_{\text{rej}} = \mathcal{A}(p_1^{\text{cal}}, \dots, p_{|\Lambda_g|}^{\text{cal}})$, while ensuring that the FWER does not exceed δ . Formally, LTT has the following guarantees.

Theorem 2. *Suppose $\mathbb{P}(p_j^{\text{cal}} \leq u) \leq u$, $u \in [0, 1]$ for all j under \mathcal{H}_j . Let \mathcal{A} be an FWER-controlling algorithm at level δ . Then $\hat{\Lambda}_{\text{rej}} = \mathcal{A}(p_1^{\text{cal}}, \dots, p_{|\Lambda_g|}^{\text{cal}})$, satisfies the following*

$$\mathbb{P}\left(\sup_{\hat{\lambda} \in \hat{\Lambda}_{\text{rej}}} \{\mathcal{R}_\ell(\hat{\lambda})\} \leq \alpha_\ell\right) \geq 1 - \delta, \quad \ell = 1, \dots, N_c. \quad (18)$$

D. Efficient Risk Control via Pareto-Testing

The LTT framework relies on the choice of FWER-controlling algorithm. A simple option is the Bonferroni correction, $\mathcal{A}(p_1^{\text{cal}}, \dots, p_{|\Lambda_g|}^{\text{cal}}) = \{\lambda_j \in \Lambda_g : p_j^{\text{cal}} < \delta/|\Lambda_g|\}$, which becomes increasingly conservative as $|\Lambda_g|$ grows, thereby reducing its statistical power, i.e., the ability to reject when null hypothesis is false. Advanced testing methods exploit prior knowledge of the structure of the configuration space to identify promising configurations that are likely to control the risks. For example, Fixed Sequence Testing (FST) [35] orders configurations from the most to the least promising and tests them sequentially until a null hypothesis fails to be rejected. However, the statistical power of methods such as FST still depends critically on correctly identifying promising configurations and determining an effective testing order, tasks that become challenging when the configuration space $|\Lambda_g|$ is large and possibly lacking structure. The difficulty intensifies further in settings that involve both constrained objectives to be controlled and unconstrained objective to be optimized.

Building on the LTT framework, Pareto-Testing [36] delivers a computationally and statistically efficient FWER-controlling algorithm that satisfies (18) and simultaneously achieves strong performance on multiple additional objective functions. The core idea is to partition the calibration set into two disjoint subsets, $\mathcal{D}_{\text{cal}} = \mathcal{D}_{\text{opt}} \cup \mathcal{D}_{\text{tst}}$, where \mathcal{D}_{opt} is used to define an ordered sequence of candidate configurations, and \mathcal{D}_{tst} is used to perform hypothesis testing. Assume N objective functions $\{\mathcal{R}_1, \dots, \mathcal{R}_N\}$, where the first N_c are constrained and the remaining $N - N_c$ are unconstrained. The set \mathcal{D}_{opt} is employed to construct the Pareto frontier

with respect to all objective functions $\{\mathcal{R}_1, \dots, \mathcal{R}_N\}$. This frontier, denoted by Λ_{par} , consists of configurations that are not *dominated* by any other configuration. Formally, for any $\lambda, \lambda' \in \Lambda_g$, we say that λ' dominates λ (denoted as $\lambda' \prec \lambda$) if $\mathcal{R}_\ell(\lambda') \leq \mathcal{R}_\ell(\lambda)$ for all ℓ and $\mathcal{R}_\ell(\lambda') < \mathcal{R}_\ell(\lambda)$ for at least one ℓ . The Pareto frontier is defined as

$$\Lambda_{\text{par}} = \left\{ \lambda \in \Lambda : \{\lambda' \in \Lambda : \lambda' \prec \lambda, \lambda' \neq \lambda\} = \emptyset \right\}. \quad (19)$$

In practice, the Pareto frontier may be obtained using standard Pareto optimization methods, including brute-force grid search (see Algorithm 5 in Appendix A-B) or multi-objective Bayesian optimization algorithms [37]. The configurations in Λ_{par} are ranked in ascending order according to their estimated p -values computed on \mathcal{D}_{opt} , after which FST is applied to the ordered set using \mathcal{D}_{tst} . As long as $p_j^{\text{tst}} < \delta$, the hypothesis \mathcal{H}_j is rejected, and the corresponding configuration λ_j is added to $\hat{\Lambda}_{\text{rej}}$. This procedure halts at the configuration for which the null hypothesis cannot be rejected. In a final step, a refined set of admissible configurations is obtained by filtering the Pareto optimal configurations over $\hat{\Lambda}_{\text{rej}}$, this time considering only the free objective functions $\{\mathcal{R}_{N_c+1}, \dots, \mathcal{R}_N\}$. The resulting subset, denoted by Λ^* , contains all validated configurations that are Pareto-optimal with respect to the free objective functions.

V. PROPOSED APPROACH

This section introduces our complementary methods, which address the multiple-source localization problem of Section II. Both methods combine generic spatial likelihood maps with risk-controlling selection methods to provide principled UQ. The first method assumes a known number of sources and uses CRC (Section IV-B) to construct tight prediction regions around each estimated position, which quantify localization uncertainty under a user-specified coverage level. The second method handles the unknown-source count setting by jointly performing source detection and localization using Pareto-Testing (Section IV-D). In this case, the objectives extend to accurately estimating the true number of active sources and constructing their corresponding prediction regions, while minimizing false detections and the total prediction area. An illustration of both methods is presented in Fig. 1.

A. Known-source count

Let $\{\mathbf{p}_{i,1}^*, \dots, \mathbf{p}_{i,K}^*\}$ denote the (unordered) set of true source DOAs for sample i . Assume that a set of K predicted directions $\{\hat{\mathbf{p}}_{i,1}, \dots, \hat{\mathbf{p}}_{i,K}\}$, together with their spatial likelihood maps $\{\Phi_i^{(1)}, \dots, \Phi_i^{(K)}\}$, is available. We employ a greedy sequential matching procedure that assigns each predicted position, in order, to its nearest unmatched true position, yielding the pairs $(\hat{\mathbf{p}}_{i,1}, \mathbf{p}_{i,1}^*), \dots, (\hat{\mathbf{p}}_{i,K}, \mathbf{p}_{i,K}^*)$. For notational simplicity indices are kept unchanged, though the k -th prediction is not necessarily matched to the k -th source. Note that alternative matching mechanisms may also be used, without affecting the risk-controlling framework proposed in the sequel.

For the k -th detected source in sample i , a prediction region $\mathcal{C}_{\lambda_k}(\hat{\mathbf{p}}_{i,k})$ is constructed using a threshold $\lambda_k \in \Lambda_k^{\text{MC}}$.

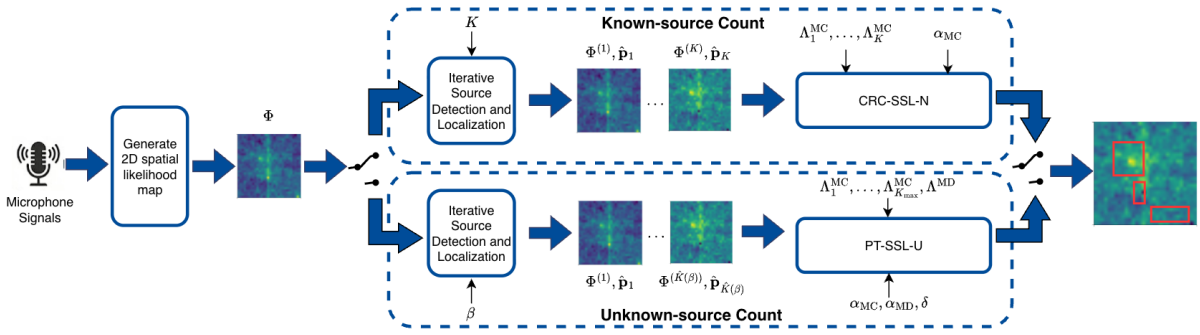


Fig. 1: Overview of the proposed UQ frameworks. For known-source count K , calibration samples with K DOAs and their likelihood maps are used, and CRC-SSL-N calibrates thresholds $(\lambda_1, \dots, \lambda_K)$ to control individual MC risks at level α_{MC} . For unknown-source count, calibration samples across detection thresholds β yield $\hat{K}(\beta)$ detections and likelihood maps, and PT-SSL-U jointly calibrates $(\lambda_1, \dots, \lambda_{K_{\max}}, \beta_{TH})$ to control MC and MD risks at levels α_{MC} and α_{MD} with high probability $1 - \delta$.

Each prediction region is defined as a spatially connected region of grid points $\mathbf{p} \in \mathcal{G}$ surrounding $\hat{\mathbf{p}}_{i,k}$. Starting from $\hat{\mathbf{p}}_{i,k}$, the set is iteratively expanded by including any grid point that is adjacent to the current set and satisfies $\Phi_i^{(k)}(\mathbf{p}) \geq \lambda_k$. Algorithm 2 provides a summary of this process.

Importantly, this formulation differs from the standard construction of CP sets or intervals. Using classification-based CP, each azimuth–elevation pair on the likelihood map can be treated as a class and included in the prediction set whenever its likelihood exceeds a threshold λ_k . However, the resulting prediction region may be non-contiguous due to spurious peaks arising from noisy and echoic environments. Moreover, in multi-source scenarios, standard CP yields only a single joint region, making it unclear how to split the region into individual sources. Alternatively, using a regression formulation, a prediction region could be defined as a fixed 2D geometric shape centered at $\hat{\mathbf{p}}_k$ (e.g., a circle or a square). However, this would impose an unrealistic assumption that the likelihood landscape follows a particular geometric structure.

A MC occurs whenever the true DOA $\mathbf{p}_{i,k}^*$ is not included in the associated prediction region. Formally, for the k -th source, define the exchangeable random variables $L_{i,k}^{MC} : \Lambda_k^{MC} \rightarrow \{0, 1\}$ for $i = 1, \dots, n + 1$,

$$L_{i,k}^{MC}(\lambda_k) = \mathbb{1}\{\mathbf{p}_{i,k}^* \notin \mathcal{C}_{\lambda_k}(\hat{\mathbf{p}}_{i,k})\}. \quad (20)$$

The corresponding empirical MC risk is

$$\hat{\mathcal{R}}_{n,k}^{MC}(\lambda_k) = \frac{1}{n} \sum_{i=1}^n L_{i,k}^{MC}(\lambda_k), \quad k = 1, \dots, K. \quad (21)$$

For each source k , we aim to construct $\mathcal{C}_{\hat{\lambda}_k}$ that guarantees the MC risk on unseen data is at most α , namely

$$\mathbb{E}[L_{n+1,k}^{MC}(\hat{\lambda}_k)] \leq \alpha, \quad k = 1, \dots, K. \quad (22)$$

In this setting, smaller thresholds produce larger prediction regions: for any $\lambda_1 < \lambda_2$, $\mathcal{C}_{\lambda_2} \subseteq \mathcal{C}_{\lambda_1}$, implying $L(\lambda_1) \leq L(\lambda_2)$ since the MC loss can only decrease as regions expand. Therefore, $L(\lambda)$ is monotone *non-decreasing* in λ and bounded by 1, satisfying the requirements of the CRC Theorem (1), up to reversed monotonicity relation. Accordingly, we obtain the following CRC selection rule for

Algorithm 2 Construction of the prediction regions $\mathcal{C}_\lambda(\hat{\mathbf{p}})$

Input: Predicted DOA $\hat{\mathbf{p}}$; likelihood map $\Phi(\mathbf{p})$; threshold λ
Output: prediction region $\mathcal{C}_\lambda(\hat{\mathbf{p}})$

- 1: Initialize $\mathcal{C}_\lambda(\hat{\mathbf{p}}) \leftarrow \{\hat{\mathbf{p}}\}$
 - 2: Initialize a queue $Q \leftarrow [\hat{\mathbf{p}}]$
 - 3: **while** Q is not empty **do**
 - 4: Pop a point \mathbf{p}' from Q
 - 5: **for** each grid point $\mathbf{p} \in \mathcal{G}$ adjacent to \mathbf{p}' **do**
 - 6: **if** $\mathbf{p} \notin \mathcal{C}_\lambda(\hat{\mathbf{p}})$ **and** $\Phi(\mathbf{p}) \geq \lambda$ **then**
 - 7: Add \mathbf{p} to $\mathcal{C}_\lambda(\hat{\mathbf{p}})$
 - 8: Push \mathbf{p} to Q
 - 9: **end if**
 - 10: **end for**
 - 11: **end while**
 - 12: **return** $\mathcal{C}_\lambda(\hat{\mathbf{p}})$
-

$\hat{\lambda}_k$ (in reverse direction relative to (14)):

$$\hat{\lambda}_k = \sup \left\{ \lambda_k \in \Lambda_k^{MC} : \hat{\mathcal{R}}_{n,k}^{MC}(\lambda_k) \leq \alpha - \frac{1-\alpha}{n} \right\}. \quad (23)$$

This establishes our ‘CRC-SSL-N’ framework, denoting CRC for SSL in the known source count setting. Finally, we define the (relative) Prediction Area (PA) incurred by source $k \in \{1, \dots, K\}$ for samples $i = 1, \dots, n + 1$ as

$$L_{i,k}^{PA}(\lambda_k) = \frac{|\mathcal{C}_{\lambda_k}(\hat{\mathbf{p}}_{i,k})|}{|\mathcal{G}|}, \quad (24)$$

where $|\mathcal{C}_{\lambda_k}(\hat{\mathbf{p}}_{i,k})|$ denotes the area of the prediction region on the likelihood map, whose total spatial support is $|\mathcal{G}|$. The overall empirical PA is given by

$$\hat{\mathcal{R}}_{n,k}^{PA}(\lambda_k) = \frac{1}{n} \sum_{i=1}^n L_{i,k}^{PA}(\lambda_k), \quad (25)$$

where small areas correspond to confident predictions, and vice versa, thereby directly quantifying predictive uncertainty.

B. Unknown-source Count

Assuming that the true number of sources K is unknown but satisfies $1 \leq K \leq K_{\max}$, we denote by $\{\mathbf{p}_{i,1}^*, \dots, \mathbf{p}_{i,K}^*\}$ the (unordered) true source DOAs of the i -th sample.

Following Algorithm 1, for each sample and every threshold $\beta \in \Lambda^{\text{MD}}$, the number of estimated sources is

$$\widehat{K}_i(\beta) = \max \left\{ k : \Phi_i^{(j)}(\hat{\mathbf{p}}_{i,j}) \geq \beta, \forall j \leq k \right\}, \quad (26)$$

with the convention that $\widehat{K}_i(\beta) = 0$ if the set is empty.

In this setting, we introduce additional loss functions aimed at reliably identifying the exact number of sources, depending on the threshold β . We define the Mis-Detection (MD) loss that quantifies the number of undetected sources. Let $\Lambda = \Lambda_1^{\text{MC}} \times \dots \times \Lambda_{K_{\max}}^{\text{MC}} \times \Lambda^{\text{MD}}$ denote an augmented configuration space, and define the sequence of random variables $L_i^{\text{MD}} : \Lambda \rightarrow \{0, \dots, K\}$ for $i = 1, \dots, n+1$, counting the number of missed sources among the K true sources

$$L_i^{\text{MD}}(\boldsymbol{\lambda}) = \max \left\{ 0, K - \widehat{K}_i(\beta) \right\} \quad (27)$$

In addition, we define the False Alarm (FA) loss as the sequence of random variables $L_i^{\text{FA}} : \Lambda \rightarrow \{0, \dots, K_{\max} - K\}$ for $i = 1, \dots, n+1$ counting the number of spurious peaks among the detected sources

$$L_i^{\text{FA}}(\boldsymbol{\lambda}) = \max \left\{ 0, \widehat{K}_i(\beta) - K \right\}. \quad (28)$$

Accordingly, we refine the definition of the MC loss since measuring coverage is meaningful only for true detected sources. Thus, we consider only predicted peaks whose likelihood exceeds the detection threshold β . For a given threshold configuration $\boldsymbol{\lambda}$, the MC loss for the k -th source is defined as

$$L_{i,k}^{\text{MC}}(\boldsymbol{\lambda}) = \mathbb{1} \left\{ \mathbf{p}_{i,k}^* \notin \mathcal{C}_{\lambda_k}(\hat{\mathbf{p}}_{i,k}) \wedge \Phi_i^{(k)}(\hat{\mathbf{p}}_{i,k}) \geq \beta \right\}, \quad (29)$$

and the overall MC loss is obtained by summing over all true detected sources

$$L_i^{\text{MC}}(\boldsymbol{\lambda}) = \sum_{k=1}^{\min\{K, \widehat{K}_i(\beta)\}} L_{i,k}^{\text{MC}}(\boldsymbol{\lambda}). \quad (30)$$

The PA loss of the i -th sample is defined as the average area over all detected source

$$L_i^{\text{PA}}(\boldsymbol{\lambda}) = \frac{1}{\widehat{K}_i(\beta)} \sum_{k=1}^{\widehat{K}_i(\beta)} \frac{1}{|\mathcal{G}|} |\mathcal{C}_{\lambda_k}(\hat{\mathbf{p}}_{i,k})|. \quad (31)$$

For $\widehat{K}_i(\beta) = 0$, the loss is set to $L_i^{\text{PA}}(\boldsymbol{\lambda}) = 0$ by convention.

With loss functions in place, the unknown-source count setting is cast into the following constrained Multi-Objective Optimization (MOO) problem:

$$\begin{aligned} \hat{\boldsymbol{\lambda}} &= \arg \min_{\boldsymbol{\lambda} \in \Lambda} (\mathcal{R}^{\text{FA}}(\boldsymbol{\lambda}), \mathcal{R}^{\text{PA}}(\boldsymbol{\lambda})) \\ \text{s.t. } &\mathbb{P}(\mathcal{R}^{\text{MD}}(\boldsymbol{\lambda}) \leq \alpha_{\text{MD}}) \geq 1 - \delta, \\ &\mathbb{P}(\mathcal{R}^{\text{MC}}(\boldsymbol{\lambda}) \leq \alpha_{\text{MC}}) \geq 1 - \delta. \end{aligned} \quad (32)$$

Namely, the goal is to identify configurations $\hat{\boldsymbol{\lambda}} \in \Lambda$ such that, with high probability $1 - \delta$, the MD and MC risks on unseen data are controlled while minimizing the PA and FA losses.

Toward this end, Pareto-Testing procedure is employed. Given a calibration set \mathcal{D}_{cal} , it is partitioned into disjoint subsets $\mathcal{D}_{\text{cal}} = \mathcal{D}_{\text{opt}} \cup \mathcal{D}_{\text{tst}}$. Using the optimization subset \mathcal{D}_{opt} , all four objective functions (both constrained and un-

Algorithm 3 PT-SSL-U: Pareto-Testing for SSL, unknown K

Input: Calibration set \mathcal{D}_{cal} ; Discrete configuration set Λ_g ;

Risk tolerance $\boldsymbol{\alpha} = (\alpha_{\text{MD}}, \alpha_{\text{MC}})$; Error significance δ .

Output: Optimal risk controlling set Λ^*

1: $(\mathcal{D}_{\text{opt}}, \mathcal{D}_{\text{tst}}) \leftarrow \text{SPLIT}(\mathcal{D}_{\text{cal}})$

// Optimization:

2: $\{\widehat{\mathcal{R}}_n^x(\boldsymbol{\lambda})\}_{x \in \{\text{MD}, \text{MC}, \text{FA}, \text{PA}\}, \boldsymbol{\lambda} \in \Lambda_g} \leftarrow \text{RISKS}(\Lambda_g, \mathcal{D}_{\text{opt}})$

3: $\Lambda_{\text{par}} \leftarrow \text{PARETO}(\{\widehat{\mathcal{R}}_n^x(\boldsymbol{\lambda})\}_{x \in \{\text{MD}, \text{MC}, \text{FA}, \text{PA}\}, \boldsymbol{\lambda} \in \Lambda_g})$

4: $p_j^{\text{opt}} \leftarrow \max_{x \in \{\text{MC}, \text{MD}\}} p(\{L_i^x(\boldsymbol{\lambda}_j)\}_{i \in \mathcal{D}_{\text{opt}}}; \alpha_x), \forall \boldsymbol{\lambda}_j \in \Lambda_{\text{par}}$

5: $\Lambda_{\text{sort}} \leftarrow (\boldsymbol{\lambda}_j : j = \text{argsort } p_q^{\text{opt}}) \quad \triangleright \text{Ascending order}$

// Hypothesis Testing:

6: $p_j^{\text{tst}} \leftarrow \max_{x \in \{\text{MC}, \text{MD}\}} p(\{L_i^x(\boldsymbol{\lambda}_j)\}_{i \in \mathcal{D}_{\text{tst}}}; \alpha_x), \forall \boldsymbol{\lambda}_j \in \Lambda_{\text{sort}}$

7: $J \leftarrow \min\{1 \leq j \leq |\Lambda_{\text{sort}}| : p_j^{\text{tst}} > \delta\} \quad \triangleright \text{FST procedure}$

8: $\hat{\Lambda}_{\text{rej}} \leftarrow \{\boldsymbol{\lambda}_j : j < J\}$

9: $\{\widehat{\mathcal{R}}_n^x(\boldsymbol{\lambda})\}_{x \in \{\text{MD}, \text{MC}, \text{FA}, \text{PA}\}, \boldsymbol{\lambda} \in \hat{\Lambda}_{\text{rej}}} \leftarrow \text{RISKS}(\hat{\Lambda}_{\text{rej}}, \mathcal{D}_{\text{tst}})$

10: $\Lambda^* \leftarrow \text{PARETO}(\{\widehat{\mathcal{R}}_n^x(\boldsymbol{\lambda})\}_{x \in \{\text{FA}, \text{PA}\}, \boldsymbol{\lambda} \in \hat{\Lambda}_{\text{rej}}})$

11: **return** Λ^*

constrained) are evaluated over a discretized configuration space $\Lambda_g \subseteq \Lambda$. We recover the Pareto frontier (19) using Algorithm 5 (Appendix A-B), yielding the set $\Lambda_{\text{par}} \subseteq \Lambda_g$ of promising configurations. Using (17), the estimated p -value associated with configuration $\boldsymbol{\lambda}_j$ is computed by

$$p_j^{\text{opt}} = \max_{x \in \{\text{MC}, \text{MD}\}} p(\{L_i^x(\boldsymbol{\lambda}_j)\}_{i \in \mathcal{D}_{\text{opt}}}; \alpha_x) \quad (33)$$

Since neither loss function is bounded by 1, the p -values are evaluated using the Waudby-Smith–Ramdas (WSR) bound [38] defined in (39) (see Appendix A-A).

To identify the rejection set $\hat{\Lambda}_{\text{rej}} \subseteq \Lambda_{\text{sort}}$, MHT procedure is performed on the testing subset \mathcal{D}_{tst} . For each configuration $\boldsymbol{\lambda}_j \in \Lambda_{\text{sort}}$, the null hypothesis

$$\mathcal{H}_j : \{\mathcal{R}^{\text{MD}}(\boldsymbol{\lambda}_j) > \alpha_{\text{MD}}\} \vee \{\mathcal{R}^{\text{MC}}(\boldsymbol{\lambda}_j) > \alpha_{\text{MC}}\} \quad (34)$$

is tested using a p -value p_j^{tst} defined analogously to (33), but evaluated on \mathcal{D}_{tst} . The FST procedure is applied, stopping at the first index j such that $p_j^{\text{tst}} > \delta$, yielding the rejection set $\hat{\Lambda}_{\text{rej}}$. Finally, a secondary filtering step is applied to $\hat{\Lambda}_{\text{rej}}$ with respect to the free objective functions (FA and PA) producing the final validated Pareto-optimal set $\Lambda^* \subseteq \hat{\Lambda}_{\text{rej}}$. Algorithm 3 summarizes the complete procedure, termed ‘PT-SSL-U’ (Pareto-Testing for SSL with unknown source count). As Pareto-Testing satisfies (18) by design, every configuration $\boldsymbol{\lambda} \in \Lambda^*$ simultaneously controls the MC and MD risks with high probability and thus constitutes a plausible solution to (32). A practitioner can then choose any $\boldsymbol{\lambda} \in \Lambda^*$, for example by minimizing PA, FA, or a weighted combination of the two.

VI. EXPERIMENTAL STUDY

We evaluate the proposed approaches on simulated data as well as real-world recordings, using the classical SRP-PHAT algorithm and the SRP-DNN model to generate 2D spatial

likelihood maps. Experiments include diverse reverberation times and varying numbers of sources, under both known and unknown source-count settings.

A. Datasets

Throughout the experiments, we employ a 12-element pseudo-spherical microphone array, consistent with the array configuration used in the LOCATA challenge [39]. Each detected source is characterized by its two-dimensional DOA $\mathbf{p}_i = [\phi_i, \theta_i]^\top$, where $\phi_i = 0$ and $\theta_i = 0$ align with the positive z - and x -axes, respectively. The 2D DOA grid is discretized with an angular resolution of 5° in both dimensions.

The SRP-DNN model is trained following [10], using randomized room dimensions, microphone-array positions, reverberation times, and Signal-to-Noise Ratio (SNR) levels. Below, we describe the data used for calibration and evaluation. All signals are analyzed in the STFT domain using a Hann window with 512 frequency bins and 50% frame overlap.

1) *Synthetic*: This dataset is used for both calibration and testing. Clean speech utterances are randomly drawn from the LibriSpeech corpus [40]. RIRs are generated based on the image-source method implemented in [41]. Two simulated rooms were considered, with reverberation time set to $T_{60} \in \{400, 700\}$ ms and fixed dimensions of $6\text{ m} \times 6\text{ m} \times 2.5\text{ m}$. The microphone signals are obtained by convolving each speech signal with the corresponding RIR, while adding Additive White Gaussian Noise (AWGN) with SNR of 15 dB. The maximum number of sources is set to $K_{\max} = 3$, with a minimum inter-source angular separation of 15° in both azimuth and elevation.

For the known-source count, we use 400 calibration samples and 100 test samples per source-count $K \in \{1, \dots, K_{\max}\}$. For the unknown-source count, we generate 1500 samples (500 for each source-count condition $K \in \{1, 2, 3\}$) and partition them into 1200 calibration samples and 300 test samples, allocated equally across the three K values.

2) *LOCATA*: We use real-world speech recordings from the LOCATA challenge dataset [39] for evaluation only in the unknown-source count setting. Calibration is carried out using LOCATA-matched synthetic data (described below). The recordings were collected in a room of size $7.1\text{ m} \times 9.8\text{ m} \times 3\text{ m}$ and a measured reverberation time of $T_{60} = 550$ ms. We consider a single evaluation test set comprising both Task-1, which contains recordings of a single active source, and Task-2, which includes scenarios with two static sources. Accordingly, the maximum number of sources is $K_{\max} = 2$. Due to the limited number of two-source static scenarios in Task-2, additional samples are generated by mixing single-source recordings from Task-1. The test set consists of 20 LOCATA recordings, comprising 10 single-source and 10 two-source scenarios.

3) *LOCATA-Matched Synthetic*: This dataset serves two purposes. It is used for calibration prior to evaluation on real-world LOCATA recordings, and it acts as a synthetic baseline for comparative performance assessment. It mirrors the LOCATA recording environment with $K_{\max} = 2$. We use 400 samples for calibration and optimization in the Pareto-Testing procedure.

B. Calibration Process

Given a set of true DOAs $\{(\mathbf{p}_{i,1}^*, \dots, \mathbf{p}_{i,K}^*)\}_{i=1}^n$, a corresponding acoustic scene is simulated for each realization. The SRP-PHAT or SRP-DNN models are then applied to generate an initial 2D spatial likelihood map Φ_i . We describe the calibration process in each setting.

1) *Known-source count*: With K known, the calibration process targets the coverage metric and is performed separately for each source $k \in \{1, \dots, K\}$. Algorithm 1 is run for exactly K iterations, yielding the estimated directions together with their associated likelihood maps. The calibration set for the k th detected source in the K -source scenario is defined as

$$\mathcal{D}_{\text{cal},K}^{(k)} = \left\{ \left((\Phi_i^{(k)}, \hat{\mathbf{p}}_{i,k}), \mathbf{p}_{i,k}^* \right) \right\}_{i \in \mathcal{D}_{\text{cal},K}}. \quad (35)$$

For each source k , the threshold space $\Lambda_k^{\text{MC}} = [0, 1]$ is discretized into 100 equally spaced values. Prediction regions $\mathcal{C}_{\lambda_k}(\hat{\mathbf{p}}_{i,k})$ are constructed using Algorithm 2, and the optimal threshold $\hat{\lambda}_k$ is selected according to (23).

2) *Unknown-source count*: Here, we perform joint detection and localization, with the objective of selecting configurations $\hat{\boldsymbol{\lambda}} = (\hat{\lambda}_1, \dots, \hat{\lambda}_{K_{\max}}, \hat{\beta})$ that solve the constrained MOO defined in (32). Assume that K_i denotes the number of active sources in the i th recording. The corresponding calibration sample consists of K_{\max} pairs of predicted source locations and their associated spatial likelihood maps, together with the ground-truth source locations

$$\mathcal{D}_{\text{cal},K_{\max}} = \left\{ \left(\left\{ (\Phi_i^{(k)}, \hat{\mathbf{p}}_{i,k}) \right\}_{k=1}^{K_{\max}}, \left\{ \mathbf{p}_{i,k}^* \right\}_{k=1}^{K_i} \right) \right\}_{i \in \mathcal{D}_{\text{cal}}}. \quad (36)$$

Similarly to the known-source-count case, for each detected peak, prediction regions are constructed iteratively using Algorithm 2.

Since the scale of Φ varies across recordings due to noise realizations and speech variability, each map is linearly normalized to the interval $[0, 1]$. We define a discrete configuration grid $\Lambda_g \subset [0, 1]^{K_{\max}+1}$, using $N = 15$ values per dimension for $K_{\max} = 3$ and $N = 35$ for $K_{\max} = 2$, resulting in $N^{K_{\max}+1}$ candidate configurations.

Finally, we note that performing calibration on the LOCATA-matched synthetic dataset and evaluating on LOCATA real recordings requires care, as the two are not exchangeable, violating a key assumption of CRC and LTT, as discussed in Appendix B-A. This induces a distribution shift in detected peak values, as shown in Fig. 4. While methods for handling non-exchangeable settings in CP have been proposed [42], [43], they are beyond the scope of this work. Instead, we adopt a simpler mitigation strategy that aligns the peak likelihood distributions (see Appendix B-A).

C. Experiments and Performance Evaluation

We present the results for each scenario, where metrics are averaged over 100 random splits for optimization (for Pareto-Testing only), calibration, and test sets.

1) *Known-source count*: In this setting, the objective is to control the MC risk at a prescribed level α_{MC} , as defined in (22), separately for each source $k \in \{1, \dots, K\}$. We

TABLE I: ‘CRC-SSL-N’ results for known $K \in \{1, 2, 3\}$ multi-source localization, using SRP-PHAT and SRP-DNN.

Localization Method	T_{60} [ms]	α_{MC}	$K = 1$		$K = 2$				$K = 3$					
			Source 1		Source 1		Source 2		Source 1		Source 2		Source 3	
			MC	PA %	MC	PA %	MC	PA %	MC	PA %	MC	PA %	MC	PA %
SRP-PHAT	400	0.100	0.102	0.15	0.098	0.16	0.105	18.89	0.097	0.16	0.100	4.25	0.098	57.63
		0.050	0.048	0.21	0.048	0.21	0.052	45.79	0.047	0.23	0.048	25.09	0.048	79.30
	700	0.100	0.094	0.19	0.097	0.20	0.106	31.43	0.094	0.22	0.096	12.66	0.101	67.17
		0.050	0.048	0.30	0.049	0.29	0.052	61.57	0.047	0.28	0.048	45.69	0.048	85.58
SRP-DNN	400	0.100	0.097	0.09	0.092	0.09	0.101	0.15	0.096	0.09	0.098	0.12	0.101	1.62
		0.050	0.052	0.12	0.044	0.12	0.051	0.19	0.045	0.13	0.047	0.17	0.049	12.17
	700	0.100	0.097	0.12	0.093	0.12	0.098	0.19	0.098	0.11	0.093	0.17	0.098	3.87
		0.050	0.047	0.17	0.049	0.18	0.051	0.29	0.050	0.14	0.045	0.23	0.048	13.81

consider significance levels $\alpha_{MC} \in \{0.1, 0.05\}$, corresponding to target coverage levels of 90% and 95%, respectively.

Table I summarizes the results obtained by applying CRC to spatial likelihood maps generated by SRP-PHAT and SRP-DNN. For both methods, the empirical coverage closely matches the prescribed nominal levels across all source counts and room conditions. A consistent trend is observed whereby higher target coverage (from 90% to 95%) and larger T_{60} values lead to systematically larger regions, reflecting increased uncertainty under stricter reliability requirements and more challenging acoustic conditions. This effect is most pronounced for SRP-PHAT. While the first detected source is localized with high confidence and compact regions, later detected sources show expanding prediction regions as reverberation increases, indicating a substantial loss of localization certainty. In contrast, SRP-DNN exhibits more stable behavior: prediction regions remain largely compact, with only mild growth as coverage level and reverberation increase. Even in challenging multi-source settings, region expansion is limited, highlighting SRP-DNN’s robustness to reverberation and source interference and its ability to maintain low localization uncertainty under stricter coverage requirements.

Fig. 2 shows the coverage regions obtained with the CRC method applied to SRP-DNN likelihood maps for $K \in \{1, 2, 3\}$ active sources under $T_{60} = 700$ ms and SNR = 15dB. The dominant source in each case has the strongest energy and an estimated DOA very close to the ground truth, yielding a highly compact prediction region. In contrast, the third source in the $K = 3$ scenario receives a noticeably larger region, despite appearing well localized in this sample, reflecting its weaker energy and the influence of residual errors from earlier source removals.

Additional experimental results are provided in Appendix B. In Appendix B-B, the CRC procedure is applied jointly across all room settings (i.e., different reverberation levels), rather than on a per-room basis. This strategy is particularly relevant when only limited calibration data are available per room, or when the target room conditions are unknown and cannot be matched to a specific calibration set. In Appendix B-C, the CRC method is replaced by the Pareto-Testing procedure in the known source-count setting, providing stronger performance guarantees with high probability.

2) *Unknown-source count*: Performance is evaluated at $\delta = 0.1$ with risk tolerances $\alpha_{MC} = \alpha_{MD} = 0.1$. After calibration, we select, among all feasible solutions in Λ^* , the configuration that minimizes the FA objective. Next, Algorithm 1 is run on the test set with the selected detection threshold $\beta_{TH} = \hat{\beta}$, and prediction regions are constructed for each detected source using Algorithm 2 and the selected thresholds $(\hat{\lambda}_1, \dots, \hat{\lambda}_{K_{max}})$. We report both the empirical average of each objective across trials, as well as, the risk violation rates P^{MC} and P^{MD} , defined as the percentage of trials (i.e. different data splits) in which the corresponding risk exceeds its prescribed limit α_{MC} and α_{MD} , respectively, which should remain below δ .

Table II reports the results for both the synthetic and LOCATA datasets. For the synthetic data, we achieve simultaneous control of the MC and MD risks, i.e., the proportion of trials in which $\hat{\mathcal{R}}^{MC}(\hat{\lambda}) > \alpha_{MC}$ or $\hat{\mathcal{R}}^{MD}(\hat{\lambda}) > \alpha_{MD}$ remains below δ . This confirms that the theoretical guarantees of our framework hold across different acoustic scenes and model types. Both methods, however, are conservative relative to the nominal risk targets when compared to CRC, as Pareto-Testing provides high-probability control over two risks, whereas CRC enforces control in expectation over a single risk. Moreover, compared to SRP-PHAT, SRP-DNN produces more distinct peaks, leading to lower FA rates and smaller PAs. Similarly to the synthetic dataset, for the LOCATA dataset both MD and MC risks are simultaneously controlled, albeit at more conservative levels, likely due to residual distribution shift effects discussed in Appendix B-A.

In addition, since large calibration datasets are often difficult to obtain, we study the impact of the calibration set size on the performance by comparing $n_{cal} \in \{600, 900, 1200\}$, with $n_{cal} = 1200$ used in the main results. Fig. 3 summarizes the results. For all calibration sizes, both MC and MD risks remain properly controlled. With $n_{cal} = 600$, the proportion of the points exceeding the risk thresholds is generally smaller than for $n_{cal} = 1200$, indicating more conservative behavior with fewer calibration samples. As n_{cal} decreases, the mean FA and PA increase slightly but remain largely stable, suggesting that using smaller calibration sets is acceptable. However, their distributions become more dispersed, reflecting increased variance due to reduced calibration data.

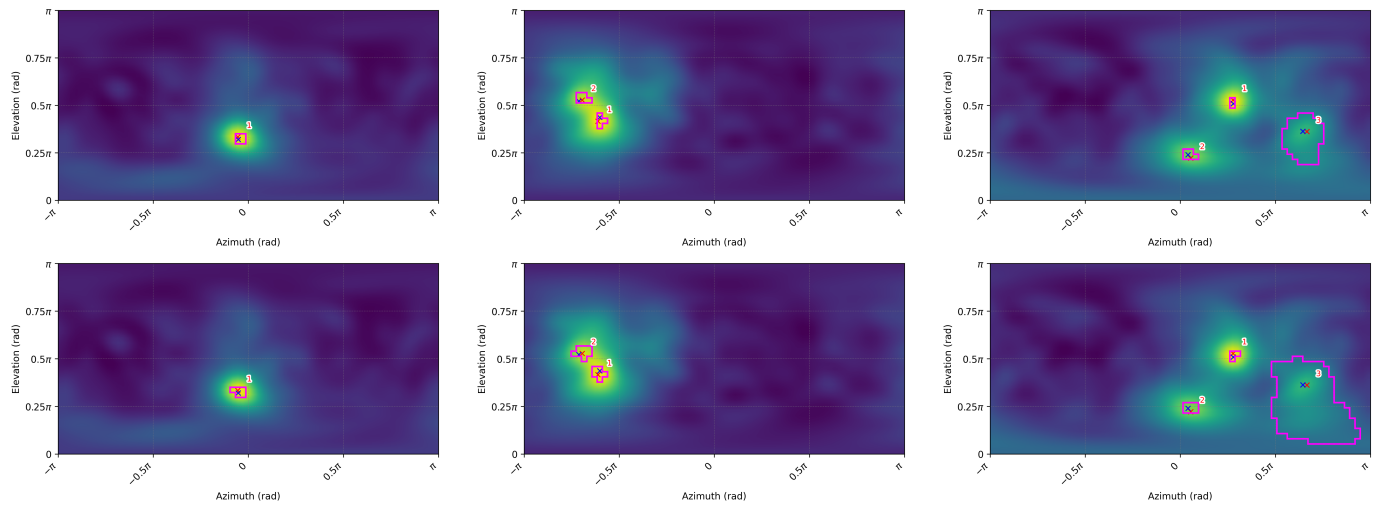


Fig. 2: ‘CRC-SSL-N’ prediction regions applied to SRP-DNN likelihood maps at 90% (top) and 95% (bottom) coverage, for $T_{60} = 700$ ms, and SNR= 15 dB. Blue and red Xs mark true and detected sources, respectively, ordered by detection. Brighter colors indicate higher likelihood. Regions expand adaptively along likelihood contours rather than fixed geometric shapes.

TABLE II: ‘PT-SSL-U’ results, with MC and MD controlled at $\alpha_{MC} = \alpha_{MD} = 0.1$ with significance level $\delta = 0.1$.

Dataset	K_{max}	T_{60} [ms]	SRP-PHAT						SRP-DNN					
			P^{MC}	MC	P^{MD}	MD	FA	PA%	P^{MC}	MC	P^{MD}	MD	FA	PA%
Synthetic	3	400	0.09	0.06	0.08	0.07	0.28	15.60	0.08	0.07	0.09	0.06	0.19	0.41
		700	0.09	0.08	0.07	0.07	0.33	19.18	0.07	0.07	0.06	0.07	0.26	0.51
LOCATA	2	550	0.03	0.05	0.09	0.06	0.26	10.20	0.05	0.05	0.09	0.05	0.02	0.25
Synthetic			0.07	0.07	0.09	0.07	0.35	6.10	0.08	0.08	0.04	0.06	0.08	0.33

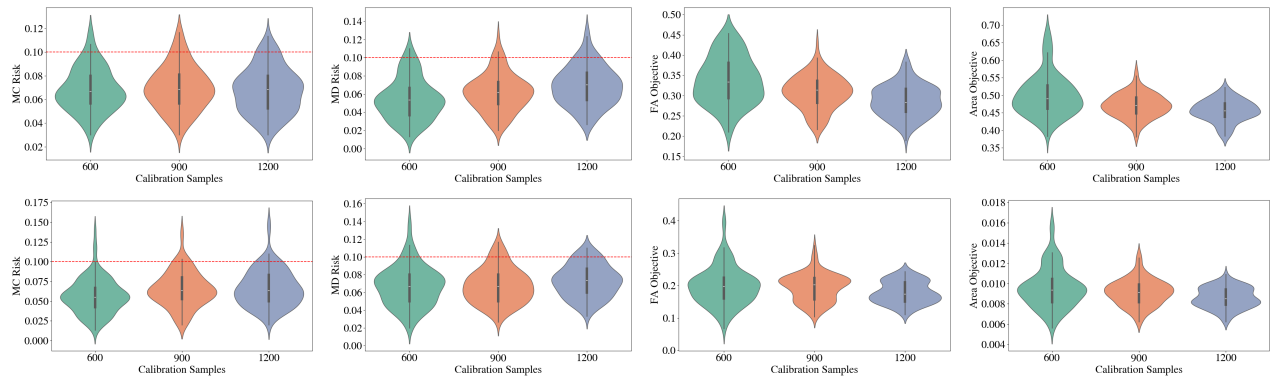


Fig. 3: ‘PT-SSL-U’ results for varying calibration-set sizes with risk tolerances $\alpha_{MC} = \alpha_{MD} = 0.1$ (dashed lines) and significance level $\delta = 0.1$. Top: SRP-PHAT. Bottom: SRP-DNN.

VII. CONCLUSION

In this work, we presented frameworks that provide finite-sample guarantees for UQ in SSL. For the known-source case, we employed CRC to construct prediction regions with controlled MC. For the unknown-source scenario, we used Pareto-Testing to obtain a statistically efficient risk-controlling configuration selection with simultaneous control of MC and MD, while encouraging minimal FA and smallest PAs among admissible configurations. Experiments on both synthetic and real-world recordings demonstrate that these guarantees are reliably maintained across diverse acoustic conditions and models. Overall, the proposed frameworks offer a practical and statistically principled approach to

provide calibrated reliability for SSL systems.

APPENDIX A
MATHEMATICAL DETAILS

A. Computation of Valid p -Values

A convenient way to compute p -values is through concentration inequalities, but their tightness depends on the underlying loss function. For binary loss functions (e.g, MC defined in (30)), the Binomial tail bound is tight. For loss function bounded in $[0, 1]$, the Hoeffding–Bentkus (HB) bound [33] provides finite-sample guarantees with strong empirical effectiveness, but for more general loss functions it yields valid p -values only asymptotically. Moreover, HB does not adapt

Algorithm 4 WSR P -Value Evaluation

Input: Collection of n i.i.d. random variables $L_i \in [A, B]$; error significance δ ; risk tolerance α .

Output: Valid p -value for the null hypothesis $\mathcal{H} : \widehat{\mathcal{R}}_n > \alpha$

```

1: for  $i = 1, \dots, n$  do
2:    $\hat{\mu}_i \leftarrow \frac{1}{2} + \frac{\sum_{j=1}^i L_j}{1+i}$ 
3:    $\hat{\sigma}_i^2 \leftarrow \frac{1}{4} + \frac{\sum_{j=1}^i (L_j - \hat{\mu}_j)^2}{1+i}$ 
4:    $\nu_i \leftarrow \min \left\{ \frac{1}{B-A}, \sqrt{\frac{2 \log(1/\delta)}{n \hat{\sigma}_{i-1}^2}} \right\}$ 
5:    $\mathcal{K}_i \leftarrow \prod_{t=1}^i \{1 - \nu_t (L_t - \alpha)\}$ 
6: end for
7:  $p \leftarrow \min_{i=1, \dots, n} \frac{1}{\mathcal{K}_i}$ 
8: return  $p$ 
    
```

to the (unknown) loss variance, leading to a loose bound. The WSR bound [38], originally developed for random variables supported on $[0, 1]$, adapts to the empirical variance and can be seamlessly extended to arbitrary finite intervals $[A, B]$ [34].

For completeness, we outline the derivation of valid p -values based on the WSR bound. Let $L_i(\boldsymbol{\lambda}) \in [0, 1]$, $i = 1, \dots, n$, be i.i.d. random variables, and consider testing the null hypothesis $\mathcal{R}(\boldsymbol{\lambda}) > \alpha$. Under the paradigm of *testing-by-betting* [44], sequential bets are placed against the null, and substantial growth of the resulting capital serves as evidence against it. Define the capital process, initialized at unit wealth, by

$$\mathcal{K}_i(\boldsymbol{\lambda}, \alpha) = \prod_{t=1}^i \{1 - \nu_t (L_t(\boldsymbol{\lambda}) - \alpha)\}, \quad i = 1, \dots, n, \quad (37)$$

where ν_i denotes the betting strategy, which depends on past loss observations $L_1(\boldsymbol{\lambda}), \dots, L_{t-1}(\boldsymbol{\lambda})$ and error significance δ . Under \mathcal{H}_0 , the process $\{\mathcal{K}_i\}$ is a nonnegative supermartingale with $\mathbb{E}[\mathcal{K}_i] \leq 1$. By Ville's inequality [45] it follows that

$$\mathbb{P} \left(\max_{i=1, \dots, n} \mathcal{K}_i(\boldsymbol{\lambda}, \alpha) \geq \frac{1}{\delta} \right) \leq \delta. \quad (38)$$

Thus, under \mathcal{H}_0 and for any betting strategy, the probability that the capital process ever exceeds $1/\delta$ is at most δ . Thus, observing $\mathcal{K}_i(\boldsymbol{\lambda}, \alpha) \geq 1/\delta$ for some i constitutes strong evidence against \mathcal{H}_0 and justifies its rejection at level δ . Since Ville's inequality in (38) can be expressed as $\mathbb{P} \left(\min_i \frac{1}{\mathcal{K}_i(\boldsymbol{\lambda}, \alpha)} \leq \delta \right) \leq \delta$, the corresponding p -value is

$$p(\boldsymbol{\lambda}, \alpha) = \min_{i=1, \dots, n} \frac{1}{\mathcal{K}_i(\boldsymbol{\lambda}, \alpha)}. \quad (39)$$

Algorithm 4 summarizes the procedure for computing WSR p -values, following [34].

B. Recovering the Pareto Optimal Front

Algorithm 5 describes the filtering procedure used to recover the Pareto-optimal set.

Algorithm 5 Recover Pareto-Optimal Set

Input: Discrete space $\boldsymbol{\Lambda}_g$; Objective functions $\{\mathcal{R}_1, \dots, \mathcal{R}_r\}$

Output: Pareto-optimal set $\boldsymbol{\Lambda}_{\text{par}}$

```

1:  $\boldsymbol{\Lambda}_o \leftarrow \boldsymbol{\Lambda}_g$ 
2: for  $\boldsymbol{\lambda} \in \boldsymbol{\Lambda}_g$  do
3:   if  $\exists \boldsymbol{\lambda}' \in \boldsymbol{\Lambda}_g \setminus \{\boldsymbol{\lambda}\}$  s.t.  $(\forall i : \mathcal{R}_i(\boldsymbol{\lambda}') \leq \mathcal{R}_i(\boldsymbol{\lambda}))$  then
4:      $\boldsymbol{\Lambda}_o \leftarrow \boldsymbol{\Lambda}_o \setminus \{\boldsymbol{\lambda}\}$ 
5:   end if
6: end for
7: return  $\boldsymbol{\Lambda}_{\text{par}}$ 
    
```

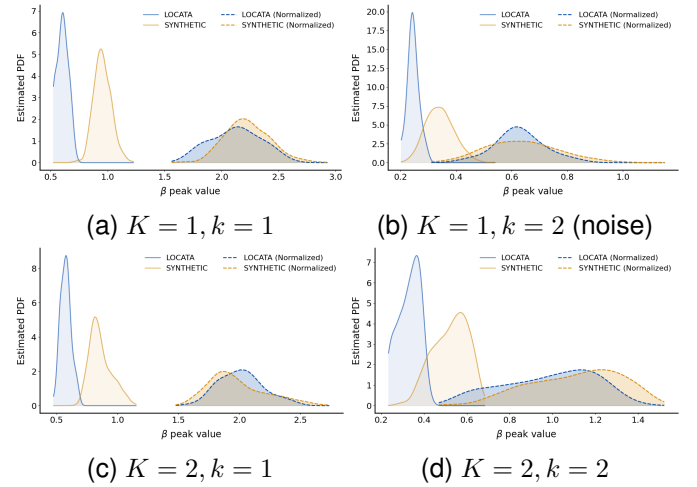


Fig. 4: Estimated PDFs of β peak values for $K_{\text{max}} = 2$.

APPENDIX B

ADDITIONAL EXPERIMENTAL DETAILS & RESULTS

A. Mitigating Simulation–Real Distribution Shifts

Despite closely matching the acoustic conditions of the LOCATA-matched synthetic dataset used for calibration with those of the real-world LOCATA recordings used for testing, a noticeable distribution shift persists in the detected peak statistics, as shown in Fig. 4. Although non-exchangeability remains, we partially mitigate this shift using an affine transformation that preserves the spatial structure of the likelihood map. Specifically, the i -th calibration map is normalized as

$$\tilde{\Phi}_i^{(k)} = \frac{\Phi_i^{(k)} - q_{0.5}(\mathcal{D}_{\text{cal}}^\Phi)}{q_{0.99}(\mathcal{D}_{\text{cal}}^\Phi) - q_{0.5}(\mathcal{D}_{\text{cal}}^\Phi)}. \quad (40)$$

where $q_\tau(\cdot)$ denotes the τ -quantile and $\mathcal{D}_{\text{cal}}^\Phi = \{\Phi_i^{(k)}\}_{i \in \mathcal{D}_{\text{cal}}, k=1}^{K_{\text{max}}}$. An analogous normalization is applied to the test likelihood maps using the test set statistics. As illustrated in Fig. 4, this normalization substantially improves alignment between the calibration and test distributions.

B. MC Risk Control Across Multiple Rooms

Controlling the MC risk simultaneously across multiple rooms is important for practical deployment, as acoustic conditions vary and per-room recalibration is often impractical. To allow robustness to such variability, we employ unified calibration and test sets spanning multiple room conditions.

TABLE III: ‘CRC-SSL-N’ controlled simultaneously across multiple rooms ($T_{60} \in \{400, 550, 700\}$ ms, SNR= 15 dB).

	α_{MC}	$K = 1$		$K = 2$				$K = 3$					
		Source 1		Source 1		Source 2		Source 1		Source 2		Source 3	
		MC	PA%	MC	PA%	MC	PA%	MC	PA%	MC	PA%	MC	PA%
SRP-	0.100	0.098	0.18	0.099	0.18	0.101	27.15	0.095	0.19	0.101	8.26	0.097	63.68
PHAT	0.050	0.047	0.27	0.045	0.25	0.050	55.66	0.043	0.27	0.051	37.78	0.049	80.82
SRP-	0.100	0.094	0.10	0.096	0.11	0.097	0.17	0.091	0.10	0.093	0.15	0.103	2.78
DNN	0.050	0.051	0.14	0.046	0.14	0.045	0.25	0.042	0.13	0.046	0.20	0.047	13.64

TABLE IV: ‘PT-SSL-N’ results in known-source count. $\alpha_{MC} = \delta = 0.1$.

T_{60} [ms]	SRP-PHAT						SRP-DNN					
	$K = 1$		$K = 2$		$K = 3$		$K = 1$		$K = 2$		$K = 3$	
	P^{MC}	PA%	P^{MC}	PA%	P^{MC}	PA%	P^{MC}	PA%	P^{MC}	PA%	P^{MC}	PA%
400	0.08	0.31	0.10	23.19	0.05	44.80	0.09	0.12	0.06	0.22	0.05	5.07
700	0.10	0.32	0.10	35.20	0.04	54.20	0.10	0.16	0.10	0.32	0.08	5.69

Specifically, the calibration and test sets comprise three simulated rooms with fixed dimensions and constant SNR, while varying the reverberation time $T_{60} \in \{400, 550, 700\}$ ms. The results are reported in Table III. As shown, the empirical coverage remains very close to the nominal level across all source counts, indicating effective control of MC risk under heterogeneous acoustic conditions. The PA falls reasonably between the values obtained for $T_{60} = 400$ ms and $T_{60} = 700$ ms reported in Table I. Note, however, that this approach provides only marginal coverage guarantees over the mixture distribution of rooms, whereas room-specific calibration yields coverage guarantees tailored to each setup individually.

C. Pareto-Testing for known-source count

We propose an alternative to the ‘CRC-SSL-N’ framework of Section V-A using Pareto-Testing, as in the unknown source count case; we refer to this variant as ‘PT-SSL-N’. The goal is to select a configuration $\lambda = (\lambda_1, \dots, \lambda_K)$ by solving the following constrained optimization problem

$$\hat{\lambda} = \arg \min_{\lambda \in \Lambda} \mathcal{R}^{PA}(\lambda) \quad \text{s.t.} \quad \mathbb{P}(\mathcal{R}^{MC}(\lambda) \leq \alpha_{MC}) \geq 1 - \delta, \quad (41)$$

where $\Lambda = \Lambda_1^{MC} \times \dots \times \Lambda_K^{MC}$. Here, we aggregate the MC and PA measures across sources, in contrast to CRC, where they are defined per source. Note also that while both approaches aim to control the MC risk at level α_{MC} , Pareto-Testing provides high-probability guarantees, whereas CRC ensures risk control only in expectation, as formalized in Theorem (1). Results for the Pareto-Testing approach are reported in Table IV. The nominal coverage level is never violated across reverberation times or localization methods. Compared to the CRC results in Table I, Pareto-Testing yields more conservative MC control and slightly larger PAs, reflecting the stronger (high-probability) guarantees it enforces.

REFERENCES

[1] C. Rascon and I. Meza, “Localization of sound sources in robotics: A review,” *Robotics and Autonomous Systems*, vol. 96, pp. 184–210, 2017.

[2] J. Benesty, “Adaptive eigenvalue decomposition algorithm for passive acoustic source localization,” *J. Acoustical Society of America*, vol. 107, pp. 384–391, 2000.

[3] M. I. Mandel, R. J. Weiss, and D. P. W. Ellis, “Model-based expectation-maximization source separation and localization,” *IEEE Transactions on Audio, Speech, and Language Processing*, vol. 18, no. 2, pp. 382–394, 2010.

[4] J. H. DiBiase, H. F. Silverman, and M. S. Brandstein, “Robust localization in reverberant rooms,” in *Microphone arrays: signal processing techniques and applications*, Springer, 2001, pp. 157–180.

[5] O. Schwartz and S. Gannot, “Speaker tracking using recursive EM algorithms,” *IEEE/ACM Transactions on Audio, Speech, and Language Processing*, vol. 22, no. 2, pp. 392–402, 2013.

[6] R. O. Schmidt, “Multiple emitter location and signal parameter estimation,” *IEEE Transactions on Antennas and Propagation*, vol. 34, no. 3, pp. 276–280, 1986.

[7] R. Roy and T. Kailath, “ESPRIT-estimation of signal parameters via rotational invariance techniques,” *IEEE Transactions on Acoustics, Speech and Signal Processing*, vol. 37, no. 7, pp. 984–995, 1989.

[8] P.-A. Grumiaux, S. Kitić, L. Girin, and A. Guérin, “A survey of sound source localization with deep learning methods,” *The Journal of the Acoustical Society of America*, vol. 152, no. 1, pp. 107–151, 2022.

[9] J. M. Vera-Diaz, D. Pizarro, and J. Macias-Guarasa, “Towards Domain Independence in CNN-based Acoustic Localization using Deep Cross Correlations,” in *28th European Signal Processing Conference (EUSIPCO)*, 2021, pp. 226–230.

[10] B. Yang, H. Liu, and X. Li, “SRP-DNN: Learning Direct-Path Phase Difference for Multiple Moving Sound Source Localization,” in *IEEE International Conference on Acoustics, Speech and Signal Processing (ICASSP)*, 2022, pp. 721–725.

[11] E. Grinstein, T. Van Waterschoot, M. Brookes, and P. A. Naylor, “The Neural-SRP Method for Positional Sound Source Localization,” in *57th Asilomar Conference on Signals, Systems, and Computers*, 2023, pp. 1318–1323.

[12] B. Shaybet, V. Tourbabin, and B. Rafaely, “SRP-PHAT-NET: A Reliability-Driven DNN for Reverberant Speaker Localization,” *arXiv preprint arXiv:2510.22682*, 2025.

[13] S. Chakrabarty and E. A. P. Habets, “Multi-Speaker DOA Estimation Using Deep Convolutional Networks Trained With Noise Signals,” *IEEE Journal of Selected Topics in Signal Processing*, vol. 13, pp. 8–21, 2019.

[14] R. Pi and X. Yu, “Uncertainty Estimation for Sound Source Localization With Deep Learning,” *IEEE Transactions on Instrumentation and Measurement*, vol. 74, pp. 1–12, 2025.

[15] A. Gammerman, V. Vovk, and V. Vapnik, “Learning by transduction,” in *Proceedings of the Fourteenth Conference on Uncertainty in Artificial Intelligence (UAI)*, vol. 14, 1998, pp. 148–155.

[16] V. Vovk, A. Gammerman, and G. Shafer, *Algorithmic learning in a random world*. Springer, 2005.

- [17] A. N. Angelopoulos, R. F. Barber, and S. Bates, “Theoretical foundations of conformal prediction,” *arXiv preprint arXiv:2411.11824*, 2024.
- [18] I. D. Khurjekar and P. Gerstoft, “Uncertainty quantification for direction-of-arrival estimation with conformal prediction,” *The Journal of the Acoustical Society of America*, vol. 154, no. 2, pp. 979–990, 2023.
- [19] B. Laufer-Goldshtein, R. Talmon, and S. Gannot, “Semi-Supervised Source Localization on Multiple-Manifolds with Distributed Microphones,” *IEEE/ACM Transactions on Audio, Speech, and Language Processing*, vol. 25, no. 7, pp. 1477–1491, 2017.
- [20] V. Rozenfeld and B. L. Goldshtein, “Conformal Prediction for Manifold-based Source Localization with Gaussian Processes,” in *IEEE International Conference on Acoustics, Speech and Signal Processing (ICASSP)*, 2025, pp. 1–5.
- [21] O. Michael and B. Laufer-Goldshtein, “Semi-supervised gnn for sound source localization with prediction intervals,” in *IEEE International Conference on Acoustics, Speech, and Signal Processing (ICASSP)*, 2026, pp. 1–5.
- [22] R. F. Barber, E. J. Candès, A. Ramdas, and R. J. Tibshirani, “Predictive inference with the Jackknife+,” *The Annals of Statistics*, vol. 49, pp. 486–507, 2021.
- [23] I. D. Khurjekar and P. Gerstoft, “Multi-source doa estimation with statistical coverage guarantees,” in *IEEE International Conference on Acoustics, Speech and Signal Processing (ICASSP)*, 2024, pp. 5310–5314.
- [24] L. Wang, T.-K. Hon, J. D. Reiss, and A. Cavallaro, “An Iterative Approach to Source Counting and Localization Using Two Distant Microphones,” *IEEE/ACM Transactions on Audio, Speech, and Language Processing*, vol. 24, no. 6, pp. 1079–1093, 2016.
- [25] A. Brutti, M. Omologo, and P. Svaizer, “Multiple source localization based on acoustic map de-emphasis,” *EURASIP Journal on Audio, Speech, and Music Processing*, vol. 2010, no. 1, p. 147495, 2010.
- [26] D. Diaz-Guerra and J. R. Beltran, “Source cancellation in cross-correlation functions for broadband multisource doa estimation,” *Signal Processing*, p. 107442, 2020.
- [27] A. N. Angelopoulos, S. Bates, M. Jordan, and J. Malik, “Uncertainty Sets for Image Classifiers using Conformal Prediction,” in *The Ninth International Conference on Learning Representations (ICLR)*, 2021.
- [28] J. Silva-Rodríguez, I. Ben Ayed, and J. Dolz, “Conformal Prediction for Zero-Shot Models,” in *Computer Vision and Pattern Recognition Conference (CVPR)*, 2025, pp. 19931–19941.
- [29] A. Fisch, T. Schuster, T. S. Jaakkola, and R. Barzilay, “Efficient Conformal Prediction via Cascaded Inference with Expanded Admission,” in *The Tenth International Conference on Learning Representations (ICLR)*, 2021.
- [30] V. Quach et al., “Conformal Language Modeling,” in *The Twelfth International Conference on Learning Representations (ICLR)*, 2024.
- [31] H. Papadopoulos, K. Proedrou, V. Vovk, and A. Gammerman, “Inductive confidence machines for regression,” in *Machine Learning: European Conference on Machine Learning (ECML)*, 2002, pp. 345–356.
- [32] A. Angelopoulos, S. Bates, A. Fisch, L. Lei, and T. Schuster, “Conformal Risk Control,” in *The Twelfth International Conference on Learning Representations (ICLR)*, 2024.
- [33] S. Bates, A. Angelopoulos, L. Lei, J. Malik, and M. Jordan, “Distribution-free, risk-controlling prediction sets,” *Journal of the ACM*, vol. 68, no. 6, pp. 1–34, 2021.
- [34] B.-S. Einbinder, L. Ringel, and Y. Romano, “Semi-supervised risk control via prediction-powered inference,” *IEEE Transactions on Pattern Analysis and Machine Intelligence*, vol. 47, no. 12, pp. 11080–11090, 2025.
- [35] A. N. Angelopoulos, S. Bates, E. J. Candès, M. I. Jordan, and L. Lei, “Learn then test: Calibrating predictive algorithms to achieve risk control,” *The Annals of Applied Statistics*, vol. 19, no. 2, pp. 1641–1662, 2025.
- [36] B. Laufer-Goldshtein, A. Fisch, R. Barzilay, and T. S. Jaakkola, “Efficiently Controlling Multiple Risks with Pareto Testing,” in *The Eleventh International Conference on Learning Representations (ICLR)*, 2023.
- [37] M. Lindauer et al., “SMAC3: A versatile Bayesian optimization package for hyperparameter optimization,” *Journal of Machine Learning Research*, vol. 23, no. 54, pp. 1–9, 2022.
- [38] I. Waudby-Smith and A. Ramdas, “Variance-adaptive confidence sequences by betting,” *arXiv preprint arXiv:2010.09686*, 2020.
- [39] H. W. Löllmann et al., “The LOCATA challenge data corpus for acoustic source localization and tracking,” in *2018 IEEE 10th sensor array and multichannel signal processing workshop (SAM)*, 2018, pp. 410–414.
- [40] V. Panayotov, G. Chen, D. Povey, and S. Khudanpur, “Librispeech: An ASR corpus based on public domain audio books,” in *IEEE international conference on acoustics, speech and signal processing (ICASSP)*, 2015, pp. 5206–5210.
- [41] D. Diaz-Guerra, A. Miguel, and J. R. Beltran, “gpuRIR: A python library for room impulse response simulation with GPU acceleration,” *Multimedia Tools and Applications*, vol. 80, no. 4, pp. 5653–5671, 2021.
- [42] R. J. Tibshirani, R. Foygel Barber, E. Candès, and A. Ramdas, “Conformal prediction under covariate shift,” *Advances in neural information processing systems (NeurIPS)*, vol. 32, 2019.
- [43] A. Farinhas, C. Zerva, D. Ulmer, and A. Martins, “Non-exchangeable conformal risk control,” in *The Twelfth International Conference on Representation Learning (ICLR)*, 2024.
- [44] A. Ramdas and R. Wang, “Hypothesis Testing with E-values,” *Foundations and Trends® in Statistics*, vol. 1, no. 1-2, pp. 1–390, 2025, ISSN: 2978-4212.
- [45] J. L. Doob, “Jean ville, étude critique de la notion de collectif,” 1939.